

Neuropilin-1-Mediated SARS-CoV-2 Infection in Bone Marrow-Derived Macrophages Inhibits Osteoclast Differentiation

Junjie Gao, Hong Mei, Jing Sun, Hao Li, Yuege Huang, Yanhong Tang, Linwei Duan, Delin Liu, Yidan Pang, Qiyang Wang, Youshui Gao, Ke Song, Jincun Zhao,* Changqing Zhang,* and Jia Liu*

In humans, severe acute respiratory syndrome coronavirus 2 (SARS-CoV-2) infection can cause medical complications across various tissues and organs. Despite the advances to understanding the pathogenesis of SARS-CoV-2, its tissue tropism and interactions with host cells have not been fully understood. Existing clinical data have revealed disordered calcium and phosphorus metabolism in Coronavirus Disease 2019 (COVID-19) patients, suggesting possible infection or damage in the human skeleton system by SARS-CoV-2. Herein, SARS-CoV-2 infection in mouse models with wild-type and beta strain (B.1.351) viruses is investigated, and it is found that bone marrow-derived macrophages (BMMs) can be efficiently infected *in vivo*. Single-cell RNA sequencing (scRNA-Seq) analyses of infected BMMs identify distinct clusters of susceptible macrophages, including those related to osteoblast differentiation. Interestingly, SARS-CoV-2 entry on BMMs is dependent on the expression of neuropilin-1 (NRP1) rather than the widely recognized receptor angiotensin-converting enzyme 2 (ACE2). The loss of NRP1 expression during BMM-to-osteoclast differentiation or NRP1 neutralization and knockdown can significantly inhibit SARS-CoV-2 infection in BMMs. Importantly, it is found that authentic SARS-CoV-2 infection impedes BMM-to-osteoclast differentiation. Collectively, this study provides evidence for NRP1-mediated SARS-CoV-2 infection in BMMs and establishes a potential link between disturbed osteoclast differentiation and disordered skeleton metabolism in COVID-19 patients.

1. Introduction

As of January 25, 2022, Severe acute respiratory syndrome coronavirus 2 (SARS-CoV-2) outbreak has caused more than 340 million infections with over 5.5 million deaths.^[1] Coronavirus disease 2019 (COVID-19) patients may develop various clinical manifestations, including severe acute pulmonary disease,^[2–4] hepatic dysfunction,^[3,4] kidney injury,^[4] heart damage,^[3,4] gastrointestinal,^[5] pancreatic symptoms,^[6] and olfactory dysfunction.^[7] However, due to the lagged, yet possibly long-lasting effects,^[8] the impact of COVID-19 on the skeleton system has not been well characterized. Bone is the major reservoir for body calcium and phosphorus.^[9] Preliminary clinical data have uncovered COVID-19-associated calcium metabolic disorders and osteoporosis.^[10,11] Importantly, severe COVID-19 patients are found to have decreased blood calcium and phosphorus levels, in comparison with moderate COVID-19 patients.^[12] These observations suggest a possible link between SARS-CoV-2 infection and damage in the skeleton system.

J. Gao, H. Li, Y. Pang, Q. Wang, Y. Gao, C. Zhang
Department of Orthopaedics
Shanghai Jiao Tong University Affiliated Shanghai Sixth People's Hospital
Shanghai 200233, China
E-mail: zhangcq@sjtu.edu.cn
H. Mei, Y. Huang, K. Song, J. Liu
Shanghai Institute for Advanced Immunochemical Studies and School
of Life Science and Technology
ShanghaiTech University
Shanghai 201210, China
E-mail: liujia@shanghaitech.edu.cn


J. Sun, Y. Tang, L. Duan, J. Zhao
State Key Laboratory of Respiratory Disease
National Clinical Research Center for Respiratory Disease
Guangzhou Institute of Respiratory Health, the First Affiliated Hospital
of Guangzhou Medical University
Guangzhou, Guangdong 510182, China
E-mail: zhaojincun@gird.cn

Y. Huang, J. Liu
Shanghai Clinical Research and Trial Center
Shanghai 201210, China

Y. Huang, J. Liu
Gene Editing Center
School of Life Science and Technology
ShanghaiTech University
Shanghai 201210, China

Y. Huang
University of Chinese Academy of Sciences
Beijing 100049, China

D. Liu
Centre for Orthopaedic Research
School of Surgery
The University of Western Australia
Nedlands, Western Australia 6009, Australia

 The ORCID identification number(s) for the author(s) of this article can be found under <https://doi.org/10.1002/adbi.202200007>.

© 2022 The Authors. Advanced Biology published by Wiley-VCH GmbH. This is an open access article under the terms of the Creative Commons Attribution-NonCommercial-NoDerivs License, which permits use and distribution in any medium, provided the original work is properly cited, the use is non-commercial and no modifications or adaptations are made.

DOI: 10.1002/adbi.202200007

Osteoclasts are one of the major cell types in the bone matrix and can mediate bone resorption. Dysfunction of osteoclasts may result in disordered bone metabolism including osteoporosis and osteopetrosis,^[13] which are characterized with abnormal blood calcium and phosphorus levels.^[14,15] Osteoclasts originate from fused bone marrow-derived macrophages (BMMs) in the presence of macrophage colony-stimulating factor (M-CSF) and receptor activator of nuclear factor kappa-B ligand (RANKL).^[16] Regulated BMM-to-osteoclast differentiation is important for maintaining the homeostasis of the skeleton system.^[17,18]

During virus infection, macrophages function as sentinel cells to restrict evading viruses and mediate inflammation response. However, during MERS-CoV infection macrophages are hijacked by the virus and support productive infection.^[19] In the case of SARS-CoV and SARS-CoV-2 infections, existing studies suggest that macrophages are abortive in virus infections and that dysregulated immune response of activated macrophages can result in rapid progression of disease.^[20,21] Nevertheless, the role of BMMs, particularly their function in bone homeostasis, during SARS-CoV-2 infection has not been fully characterized. Intriguingly, while macrophages from lymph node subcapsular and splenic marginal zone in COVID-19 patients express SARS-CoV-2 entry receptor ACE2,^[22] most tissue-resident macrophages from human have little expression of ACE2.^[21] Particularly, ACE2 has very low expression in bone marrow cells.^[23] These studies reveal largely undefined interaction networks between SARS-CoV-2 and BMMs.

In this study, we investigated the interactions between SARS-CoV-2 and BMMs using mouse models and ex vivo cultured BMMs. We found that pseudotyped and authentic SARS-CoV-2 virus could efficiently infect BMMs via an NRP1-dependent manner and disrupt BMM-to-osteoclast differentiation.

2. Results

2.1. SARS-CoV-2 Infects Femoral BMMs in Mouse Model

As there is currently no established SARS-CoV-2 infection model for the skeleton system, we employed a previously established Ad5-hACE2 mouse model.^[24] In this model, adenovirus carrying human ACE2 (hACE2) was intranasally administrated to BALB/c mice at 5 days prior to SARS-CoV-2 infection. Once hACE2 expression in mouse lung was confirmed, SARS-CoV-2 was intranasally administrated and incubated for 2 days (Figure 1A). SARS-CoV-2 infection in bone marrow was confirmed by RT-qPCR quantification of the expression of nucleocapsid protein (Figure 1B). We then collected and processed the femur (Figure 1C) for in situ immunofluorescence analysis. It was found that SARS-CoV-2 could infect BMMs across different femoral segments, as evidenced by the co-localization of viral nucleocapsid protein and macrophage marker F4/80^[25] (Figure 1D). These results provided evidence for the in vivo infection of authentic SARS-CoV-2 in BMMs.

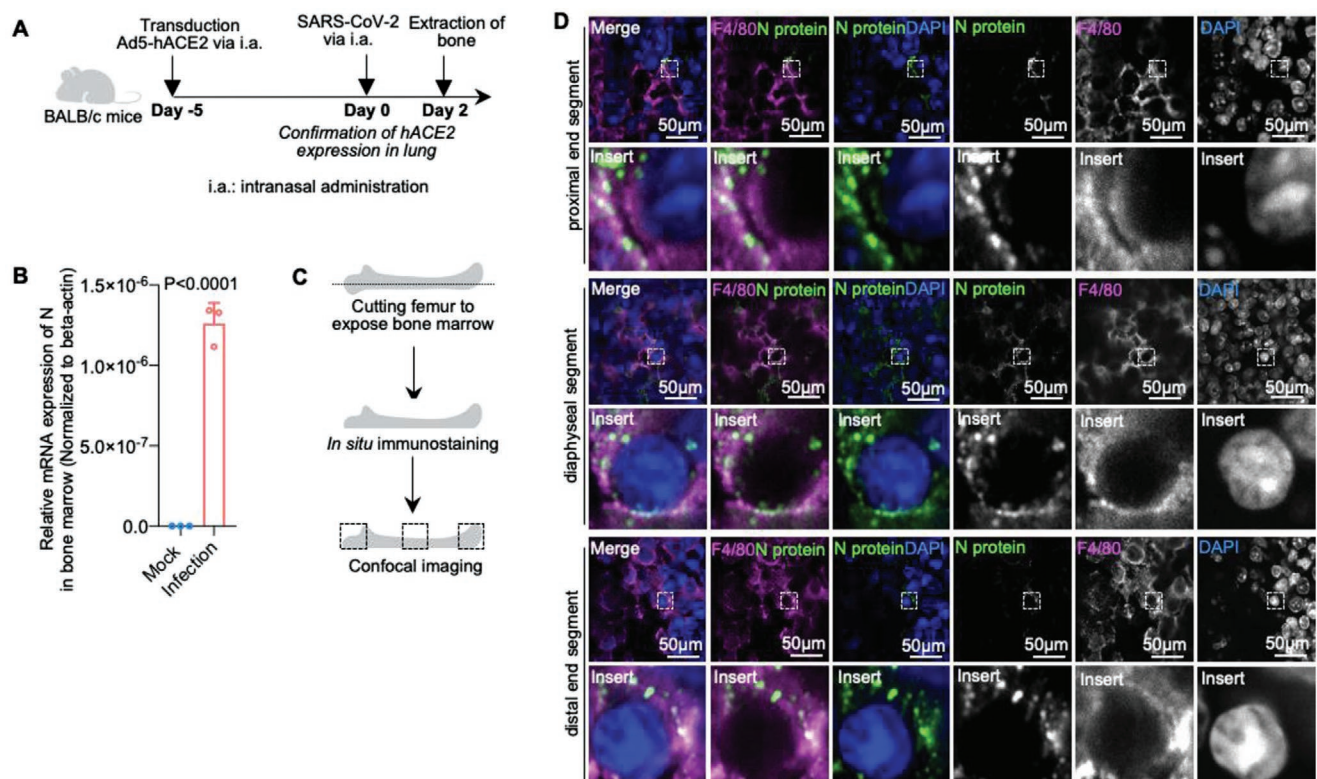


Figure 1. The in vivo infection of BMMs in Ad5-hACE2 transduced mouse model with wild-type authentic SARS-CoV-2. A) Schematic illustration of experimental procedures. B) RT-qPCR quantification of the expression of N gene in bone marrow cells. C) Experimental procedure for processing bone tissues for confocal imaging. D) In situ immunofluorescence images showing the infection of SARS-CoV-2 in BMMs from different femoral segments. SARS-CoV-2 nucleocapsid protein (N protein) and macrophage major marker F4/80 are immunostained.

2.2. Authentic SARS-CoV-2 Infects Ex Vivo Cultured BMMs

To determine the infectivity of authentic SARS-CoV-2 in BMMs, we established BMMs ex vivo culture^[26,27] (Figure S1A,B, Supporting Information) and analyzed the expression of nucleocapsid protein in control and infected ex vivo BMMs. Immunofluorescence studies confirmed the infection of mouse BMMs (mBMMs) by authentic SARS-CoV-2, as shown by the expression of nucleocapsid protein in (Figure 2A). Using SMART transcriptomic analysis (Figure S2A, Supporting Information), we found that SARS-CoV-2 genes were expressed in infected BMMs with nucleocapsid gene bearing the highest expression (Figure S2B, Supporting Information). The expression of nucleocapsid gene was subsequently verified by RT-qPCR (Figure 2B) and immunoblotting (Figure 2C).

We next analyzed the effects of authentic SARS-CoV-2 infection on the gene expression profile of mBMMs and found that 609 genes were upregulated and 1888 genes downregulated using a cutoff of 2-fold and a *p* value of less than 0.05 (Figure S2B,C, Supporting Information). Gene ontology (GO) enrichment analysis of significantly regulated genes uncovered items of immune response to viral infection (Figure 2D).

Notably, macrophage chemotaxis/differentiation and osteoclast differentiation-related genes were significantly affected (Figure S2D, Supporting Information). It was found that *Pf4* and *Lgals3* exhibited greatest difference in macrophage related genes upon SARS-CoV-2 infection (Figure 2E,F). Importantly, several osteoclast-related genes were found to be affected, among which *Tnf*, *Trem2*, *Trf*, *Csf1*, and *Ccn4* displayed greatest change (Figure 2G,H). These results demonstrated that authentic SARS-CoV-2 infection had a global impact on the gene expression profile of macrophages and suggested a possible role of SARS-CoV-2 infection on BMM differentiation toward osteoclasts. Nevertheless, we found that authentic SARS-CoV-2 infection in mBMMs yielded no detectable productive virus (Figure S3A,B, Supporting Information), which is consistent with the results of SARS-CoV infection in macrophages.^[28,29]

2.3. Establishment of SARS-CoV-2 Pseudovirus Infection System in BMMs

A key step during SARS-CoV-2 infection in mBMMs is virus entry. To dissect essential host factors during this process,

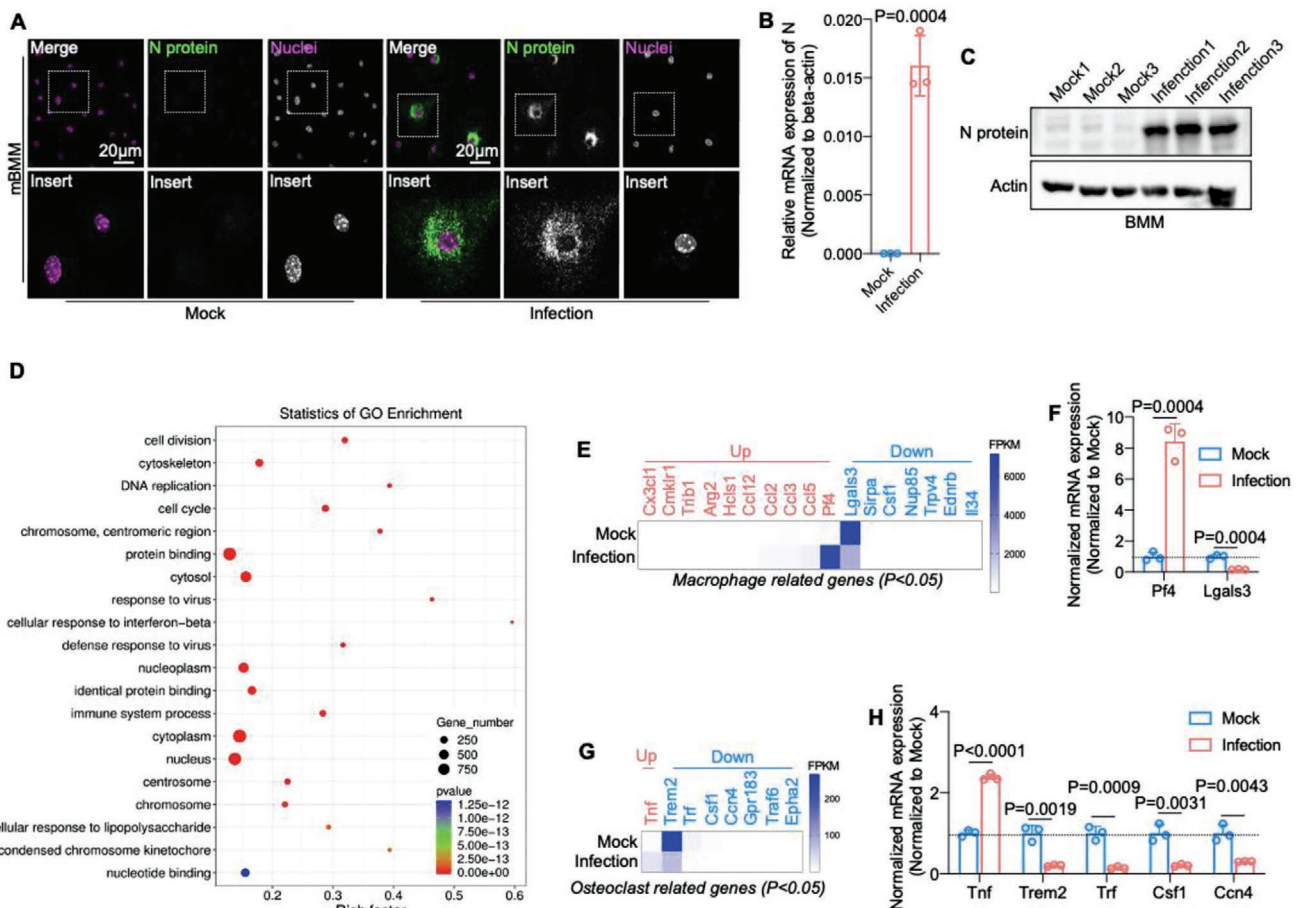


Figure 2. Authentic SARS-CoV-2 infects bone marrow-derived macrophages (BMMs). Immunofluorescence, RNA-Seq, RT-qPCR, and immunoblotting analysis of SARS-CoV-2 infection in mouse BMMs. A) Confocal images showing the infection of SARS-CoV-2 in mouse BMMs. B) RT-qPCR results of nucleocapsid gene expression. C) Immunoblotting result of nucleocapsid protein expression. D) Top 20 enriched gene ontology (GO) terms. E,F) Altered expression of macrophage-related genes. G,H) Altered expression of osteoclast-related genes. Transcriptomic analyses (E, G). RT-qPCR quantification (F and H).

we established a lentivirus-based pseudovirus containing SARS-CoV-2 spike protein, where tdTomato was included as the transgene for evaluation of virus internalization (Figure S4A,B, Supporting Information). To determine whether SARS-CoV-2 pseudovirus could infect ex vivo cultured mBMMs, we conducted flow cytometry experiments and found that $\approx 45\%$ mBMMs were tdTomato positive, suggesting of high infection efficiency (Figure S4C, Supporting Information). We then conducted RT-qPCR using primers targeting the open reading frame (ORF) region of tdTomato, which could detect the expression of tdTomato, and primers targeting EF-1a promoter, which could only detect pseudoviral genome (Figure S4A, Supporting Information). The RT-qPCR results revealed significantly higher level of tdTomato than EF-1a (Figure S4D,E, Supporting Information), suggesting successful viral infection and transcription of transgene in both human BMMs (hBMMs) and mBMMs. Furthermore, to examine whether SARS-CoV-2 pseudovirus entry was dependent on the viral spike protein, we performed neutralizing experiments using an antibody against the spike protein S1 subunit. RT-qPCR analysis of tdTomato expression showed that anti-S1 antibody significantly reduced the infection of SARS-CoV-2 pseudovirus in BMMs (Figure S4F, Supporting Information). Collectively, the above results suggested a spike protein-dependent infection of SARS-CoV-2 pseudovirus in BMMs.

2.4. Characterization of SARS-CoV-2 Pseudovirus Infection in BMMs Using Single-Cell RNA Sequencing

Next we performed pseudovirus infection in mBMM that were isolated from the bone marrow of 1- and 18-month mice for single-cell RNA sequencing (scRNA-Seq) analysis. We classified cell groups according to the expression of marker genes, and found that macrophages were the major infected cell type (Figure 3A,B and Figure S5A–C, Supporting Information). By re-clustering tdTomato-positive cells, we found that macrophages, neutrophils, fibroblasts, monocytes, DCs, T cells, and B cells were all permissive to the pseudovirus (Figure 3C–E and Figure S5D–F, Supporting Information). Furthermore, we found that pseudovirus-infected macrophages could be grouped into 10 clusters (Figure 3F and Figure S5G–I, Supporting Information). Among these cell types, cluster 7 macrophage, defined as Cx3cr1⁺Ccr2⁺ (Figure S5I, Supporting Information), had the highest infection rate (Figure 3G,H). In consistency with the high infection rate, gene enrichment analysis showed that Cx3cr1⁺Ccr2⁺ cluster 7 subset had enrichment in COVID-19 and osteoclast differentiation-related genes (Figure 3I and Figure S5J, Supporting Information). These results uncovered a possible link between SARS-CoV-2 infection in BMMs and COVID-19 or osteoclast differentiation.

2.5. Correlation of NRP1 Expression and SARS-CoV-2 Infection in BMMs

Although ACE2 is a widely recognized entry receptor for SARS-CoV-2, we found in this study that ACE2 had little expression in BMMs directly isolated from flushed mouse bone marrow (Figure 4A,B and Figure S6A–D, Supporting Information) or

in ex vivo cultured hBMMs and mBMMs (Figure 4C,D). These results indicated that other proteins might function to facilitate SARS-CoV-2 entry in BMMs. It has been reported that the S1 subunit of spike protein can bind NRP1 through CendR peptide (Figure S4A, Supporting Information) and that NRP1 can facilitate the entry of SARS-Cov-2.^[30,31] Intriguingly, we found that NRP1 was highly expressed in both bone marrow-flushed BMMs and ex vivo cultured BMMs (Figure 4B). Sequence alignment and structural analysis showed that human (PDB ID: 7JJC) and mouse (PDB ID: 4GZ9) NRP1 shared remarkable similarity (Figure 4E,F), consistent with the high infection efficiency of SARS-CoV-2 in both hBMMs and mBMMs. Particularly, the CendR motif from the S1 subunit of SARS-CoV-2 spike protein^[31,32] in human NRP1b1-S1 complex could be well docked into the b1 domain^[31] of the superimposed mouse NRP1 structure (Figure 4E).

We then employed Ad5-hACE2 mouse model to understand the in vivo relevance of NRP1 expression and SARS-CoV-2 infection in BMMs. Similar to aforementioned mouse studies, the femoral segments of infected mice were isolated and analyzed with in situ immunofluorescence. We found that SARS-CoV-2 nucleocapsid proteins were co-localized with NRP1 on F4/80-positive femoral BMMs (Figure 4G). These results provided in vivo evidence for the correlation of NRP1 expression and SARS-CoV-2 infection in BMMs.

2.6. NRP1 Mediates Pseudotyped and Authentic SARS-CoV-2 Infection in mBMMs

In pseudovirus-treated mBMMs, NRP1 expression was found to be highly correlated with tdTomato expression (Figure 5A,B). To assess the effects of NRP1 on the entry of SARS-Cov-2, we performed neutralizing experiments using recombinant spike protein S1 subunit. It is known that S1 subunit can bind both ACE2 and NRP1 through RBD and CendR peptide respectively.^[30,31,33] We found that the presence of S1 subunit significantly reduced the infection of pseudovirus (Figure 5C) in BMMs, as determined by RT-qPCR quantification of tdTomato expression.

To exclude the interference of ACE2 during SARS-CoV-2 infection in BMMs, we further examined the effects of recombinant S1-RBD domain, which was supposed to only interact with ACE2, on pseudovirus infection. RT-qPCR showed that RBD domain did not block pseudovirus infection (Figure 5D), suggesting a dispensable role of ACE2–RBD interaction during SARS-CoV-2 infection in BMMs. To further validate the essentiality of NRP1 expression for SARS-CoV-2 pseudovirus infection, we employed small-hairpin RNA (shRNA) to knock down NRP1 (Figure 5E). RT-qPCR quantification of tdTomato expression revealed suppressed pseudovirus infection upon NRP1 knockdown (Figure 5F). Collectively, these results on pseudovirus suggested that NRP1 played an important role in facilitating SARS-CoV-2 entry in mBMMs.

Similarly, the blockade of NRP1, but not ACE2, could reduce the infectivity of authentic SARS-CoV-2 in mBMMs. The addition of spike protein S1 domain inhibited the infection of authentic virus, as determined by RT-qPCR quantification of nucleocapsid and spike protein expression (Figure 5G,H). By contrast, spike protein RBD domain did not reduce authentic virus infection (Figure 5I,J). These results strongly supported that NRP1 but not ACE2 mediated the entry of SARS-CoV-2 in BMMs.

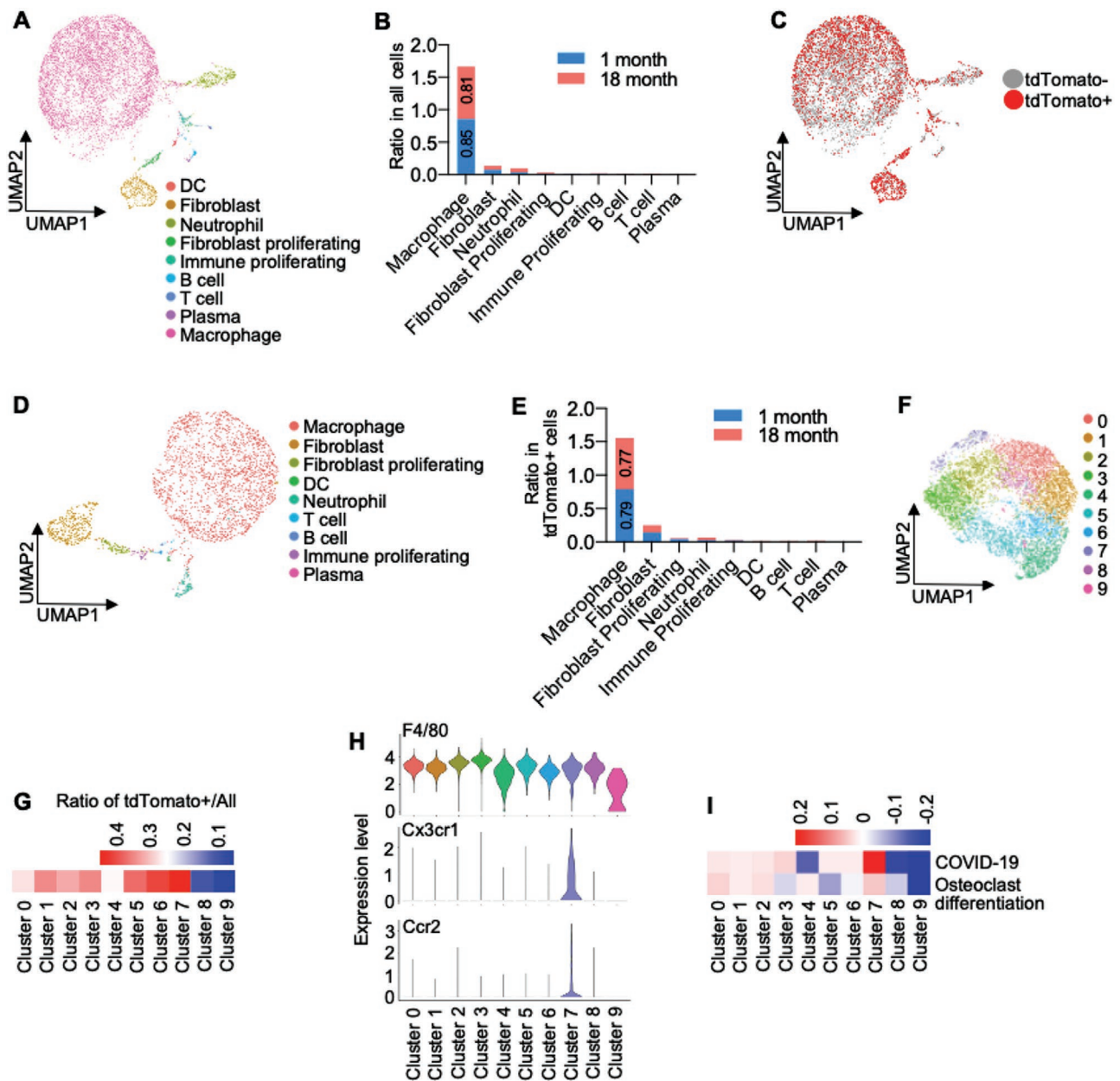


Figure 3. SARS-CoV-2 pseudovirus infects human and mouse BMMs in ex vivo culture. A) Overview of the cell clusters in integrated cell population. B) Analysis of cell type ratio, showing that macrophages are the predominant population. C) Analysis of SARS-CoV-2 pseudovirus-infected and uninfected cells, determined by tdTomato transgene expression. D) Re-clustering of tdTomato-positive cells and E) cell number quantitation, showing that macrophages are the predominant population in SARS-CoV-2 pseudovirus-infected cells. (F and G), Re-cluster of macrophages. F) Cell clusters and analysis of SARS-CoV-2 pseudovirus-infected and -uninfected cells, determined by tdTomato transgene expression. G) Cluster 7 shows the highest efficiency of SARS-CoV-2 pseudovirus infection. H) Features of cluster 7. I) Cluster 7 exhibits highest correlation with COVID-19 and osteoclast differentiation.

2.7. BMMs and Brain Macrophages Have Distinct NRP1 Expression Profiles

It is known that NRP1 had important function in central nervous system (CNS).^[34] Recent studies highlight a possible role of NRP1 in facilitating SARS-CoV-2 spreading from olfactory bulb to brain.^[30] To understand the specificity of SARS-CoV-2 infection in brain and bone marrow macrophages, it could be interesting to characterize NRP1 expression in both

macrophage populations. As age-related mortality has been observed in COVID-19 patients,^[35] we sought to analyze macrophages from mice of different ages. We found that NRP1 expression in brain macrophages was remarkably increased during brain maturation and aging (Figures S7A–D and S8A, Supporting Information). By contrast, NRP1 expression in both in vivo isolated BMMs and ex vivo cultured BMMs had minimum difference during aging (Figure S8B,C, Supporting Information). Importantly, the constant NRP1 expression in

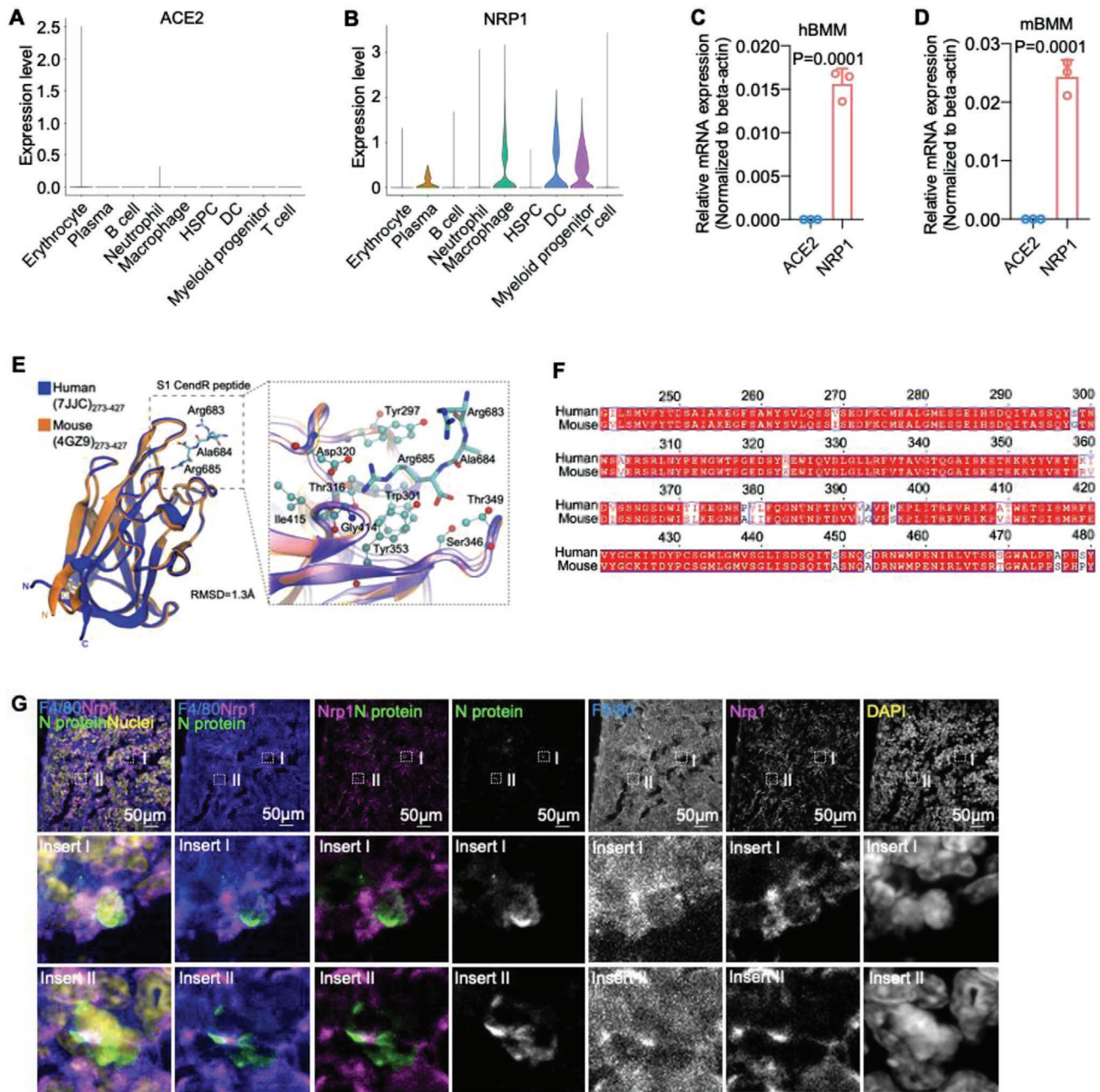


Figure 4. NRP1 but not ACE2 is expressed in BMMs. Single-cell transcriptome analysis of BMMs directly isolated from 1-, 6- or 20-month mice. Violin plot showing the expression of A) ACE2 and B) NRP1 in each cell type. RT-qPCR quantification of ACE2 and NRP1 expression in cultured C) hBMMs and D) mBMMs. E) Human NRP1b1-S1 CendR peptide complex (PDB ID: 7JJC) superposed with mouse NRP1b1 (PDB ID: 4GZ9). Binding peptide is shown in stick representation. RMSD, root mean square deviation. Enlarged view highlights the binding of S1 CendR peptide. F) Amino acid sequence alignment of human and mouse NRP1b1. G) In situ immunofluorescence images showing the co-localization of SARS-CoV-2 nucleocapsid protein and NRP1 in F4/80-positive BMMs in a mouse model with SARS-CoV-2 beta strain (B.1.351).

the BMMs from neonatal (1 month) and aged (18 month) mice was consistent with the similar infectivity of SARS-CoV-2 pseudovirus in these two types of BMMs (Figure S8D, Supporting Information). The difference in programmed time course of NRP1 expression between brain macrophages and BMMs may render BMMs a particularly vulnerable class of tissue-resident macrophages in SARS-CoV-2 infection.

2.8. Decreased SARS-CoV-2 Pseudovirus Infection in mBMM-Derived Osteoclasts Is Associated with the Loss of NRP1 Expression

BMMs are the main progenitors of osteoclasts.^[16] To investigate the infectivity of SARS-CoV-2 on macrophages at different stages during BMM-to-osteoclast differentiation, we infected

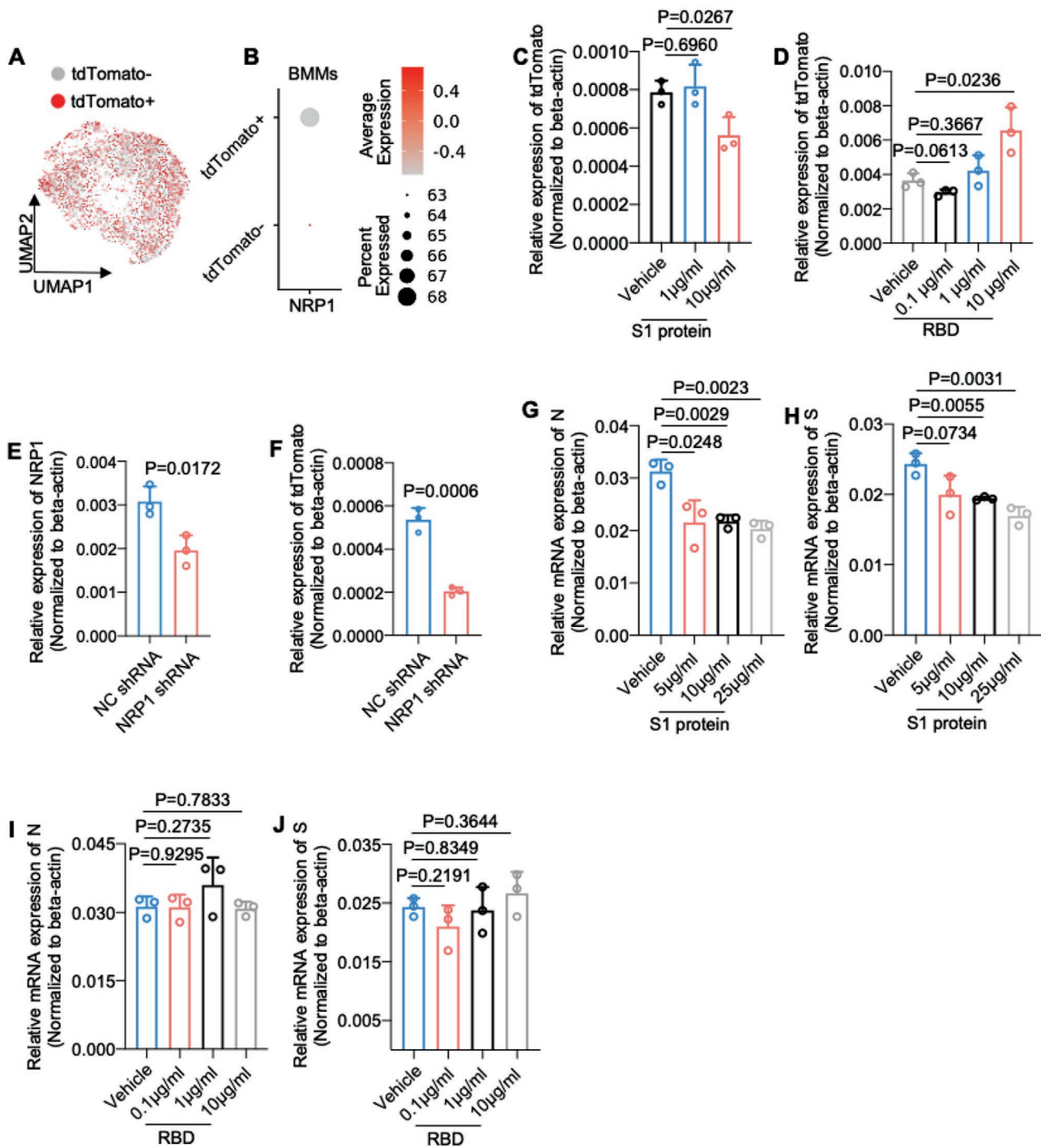


Figure 5. NRP1 facilitates pseudoviral and authentic SARS-CoV-2 infection in mBMMs. scRNA-Seq analysis of pseudoviral SARS-CoV-2-treated mBMMs. A) UMAP of tdTomato positive and negative mBMMs. B) NRP1 expression in tdTomato positive and negative mBMMs. RT-qPCR quantification of tdTomato expression, determining the effects of C) S1 subunit and D) S1-RBD domain on SARS-CoV-2 pseudovirus infection in mBMMs respectively. Evaluation of NRP1 knockdown on SARS-CoV-2 pseudovirus infection in mBMMs. E) RT-qPCR analysis of the efficiency of NRP1 knockdown. F) RT-qPCR quantification of tdTomato expression, determining the effects of NRP1 knockdown on virus infection. RT-qPCR results showing the effects of G,H) S1 subunit and I,J) RBD domain on the infection of authentic SARS-CoV-2 in BMMs, as determined by the expression of nucleocapsid (G, I) and spike (H, J) protein. The data are represented as mean \pm SD ($n = 3$) (C–J). Statistical difference is determined using two-tailed Student's *t* test.

BMMs from 1-month and 18-month mice with SARS-CoV-2 pseudovirus at the progenitor stage without RANKL stimulation, during differentiation at day 3 after RANKL stimulation,

and upon maturation at day 8 after RANKL stimulation, respectively (Figure 6A). The cell culture samples were harvested at 24 h after pseudovirus infection. TRAP staining (Figure S9A,

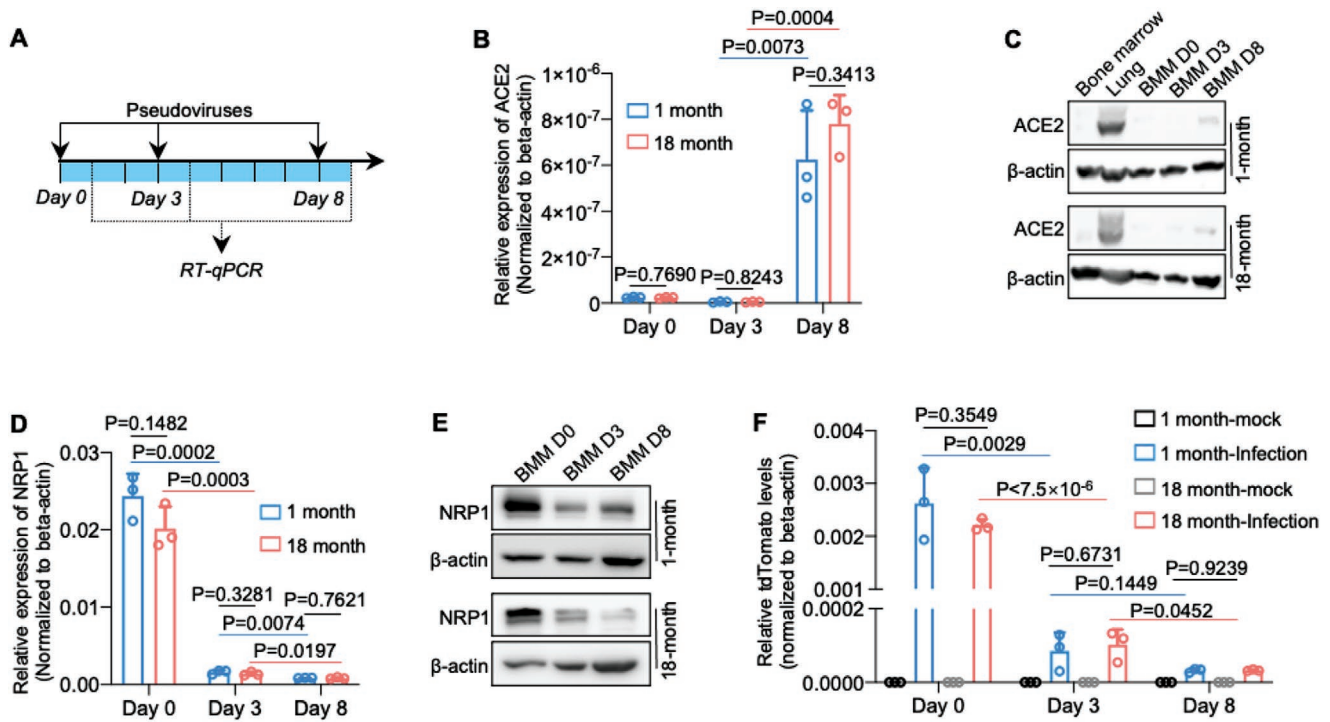


Figure 6. Decreased SARS-CoV-2 infection in mBMM-derived osteoclasts is associated with the loss of NRP1 expression. A) Flowchart showing the procedure of BMM-osteoclast differentiation, pseudovirus infection and RT-qPCR quantification. B,D) RT-qPCR quantification of ACE2 and NRP1 expression in BMMs (Day 0), deafferenting osteoclasts (Day 3) and mature osteoclasts (Day 8). C,E) Immunoblotting of ACE2 and NRP1 expression in BMMs (Day 0), differentiating osteoclasts (Day 3), and mature osteoclasts (Day 8). F) RT-qPCR quantification of SARS-CoV-2 pseudovirus infection in BMMs (Day 0), differentiating osteoclasts (Day 3), and mature osteoclasts (Day 8), determined by tdTomato transgene expression.

Supporting Information) and RT-qPCR quantification of osteoclast marker genes (Figure S9B–E, Supporting Information) confirmed successful establishment of BMM-to-osteoclast differentiation. While ACE2 expression was increased in mature osteoclasts (Figure 6B,C), NRP1 expression was markedly decreased in differentiating and mature osteoclasts (Figure 6D,E). Notably, pseudovirus infection appeared to be correlated with the expression of NRP1 during differentiation, where the infection rate gradually decreased during the progress of BMM-to-osteoclast differentiation (Figure 6F). Additionally, NRP1 expression and the infectivity of pseudovirus had no significant difference between macrophages from neonatal (1 month) and aged (18 month) mice (Figure 6D,F). Differentiation-related infection was further confirmed by immunofluorescence experiments where higher tdTomato fluorescence was detected in BMMs than in differentiating or mature osteoclasts (Figure S10, Supporting Information). In addition, we found that BMMs expressed cathepsins B and L (Ctsb and Ctsl) but not TMPRSS2 (Figure S11A–C, Supporting Information) for the priming of SARS-CoV-2.^[36–38] Interesting, Ctsb and Ctsl decreased during aging or BMM-to-osteoclast differentiation (Figure S11D–G, Supporting Information). The expression profile of host proteases might also contribute to receptor selectivity of SARS-CoV-2. Collectively, these results showed that the reduced infectivity of SARS-CoV-2 during BMM-to-osteoclast differentiation may be a result of decreased NRP1 expression.

2.9. Authentic SARS-CoV-2 Infection in BMMs Disrupts BMM-to-Osteoclast Differentiation Ex Vivo and In Vivo

To investigate the potential impact of SARS-CoV-2 infection on bone homeostasis, we sought to evaluate the effects of authentic virus on BMM-osteoclast differentiation. We stimulated the SARS-CoV-2-infected BMMs with RANKL for 3 or 8 days and then quantified osteoclast differentiation related markers using RT-qPCR. We found that the expression of marker genes Calcitonin, Stamp, Trap and Mmp9 was increased in RANKL treated group in the absence of authentic virus (Figure 7A–D). By contrast, in SARS-CoV-2-infected groups very limited increase of expression was observed with the marker genes (Figure 7A–D). Consistent results were obtained in BMMs isolated from neonatal (1 month) and aged (18 months) mice (Figure 7A–D). These results suggested that SARS-CoV-2 infection impeded BMM-osteoclast differentiation under ex vivo conditions.

We next sought to understand the in vivo relevance between SARS-CoV-2 infection in BMMs and osteoclast differentiation. In a recent study, K18-hACE2 transgenic mice were used to understand SARS-CoV-2 infection in macrophages.^[39] Because we have clearly demonstrated that NRP1, rather than ACE2, mediates SARS-CoV-2 infection in BMMs, the use of hACE2 transgenic or transduction mouse model may be misleading in understanding the correlation between SARS-CoV-2 infection in BMMs and osteoclast differentiation. Therefore, in the present study we use SARS-CoV-2 beta strain (B.1.351) that had been

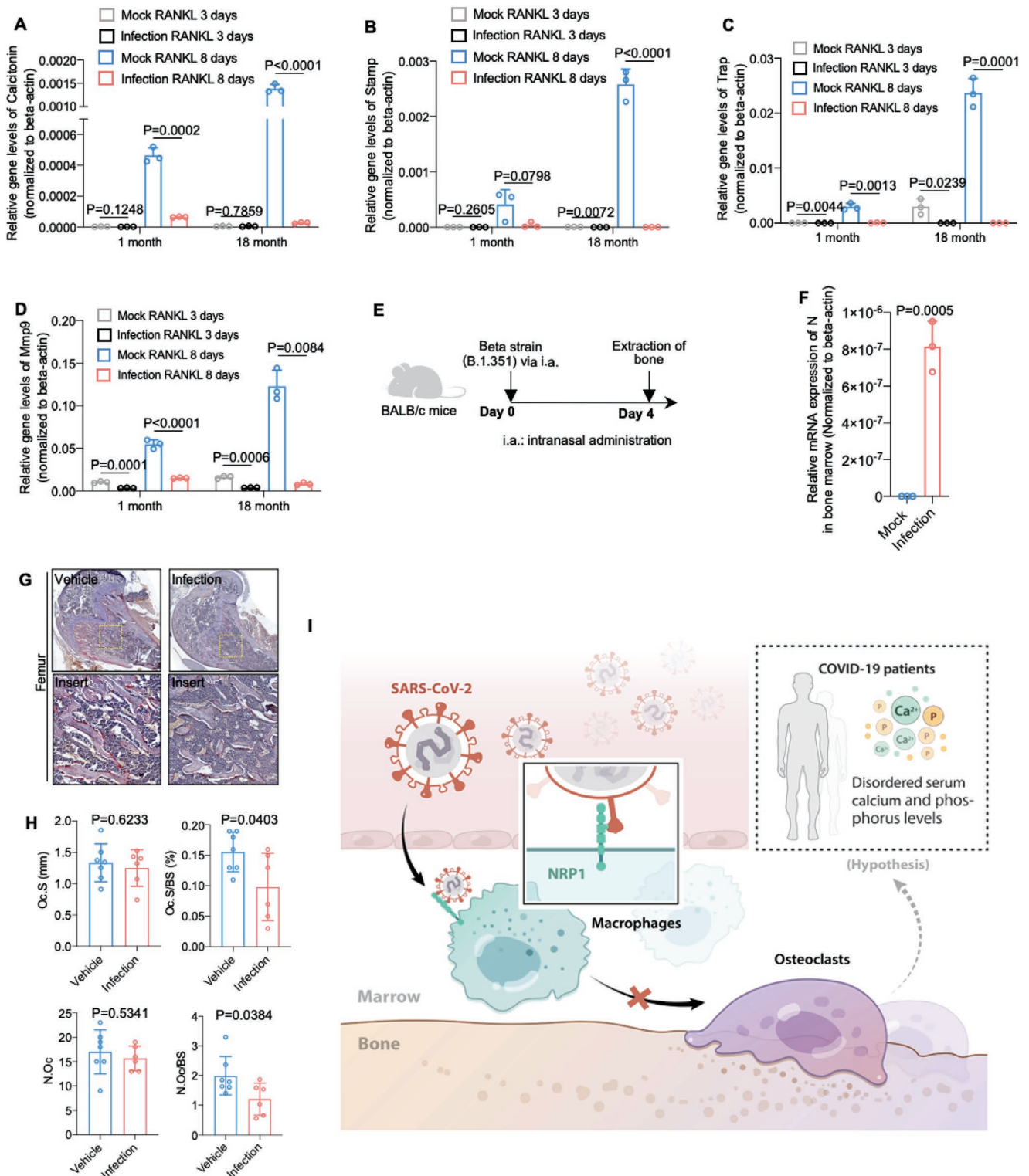


Figure 7. SARS-CoV-2 infection inhibits mBMM to osteoclast differentiation. A–D) RT-qPCR quantification showing the effects of authentic SARS-CoV-2 on BMM-to-osteoclast differentiation under ex vivo conditions. Analysis of the effects of SARS-CoV-2 infection on BMM-to-osteoclast differentiation in an animal model with the beta strain virus (B.1.351). E) Schematic illustration of experimental procedures. F) RT-qPCR validation of the expression of N gene in bone marrow cells. G) TRAP staining of femoral bone samples. H) Quantitation of osteoclast surface (Oc.S), osteoclast surface per bone surface (Oc.S/BS), number of osteoclasts (N.Oc) and number of osteoclasts per bone surface (N.Oc/BS). The data are shown as mean \pm SD. Statistical difference is determined using two-tailed Student's *t* test (A–D, F). I) Proposed model for the effects of NRP1-mediated SARS-CoV-2 infection on the homeostasis of the skeleton system.

reported to be capable of infecting unmodified Balb/c mice.^[40] The beta strain virus (B.1.351) could efficiently infect mice without the need of hACE2 transduction or expression, as evidenced by the expression of nucleocapsid protein (Figure 7E,F). Similar to the procedure in Ad-hACE2 model, the femoral and tibial bone samples of these mice were processed and stained for the expression of tartrate resistant acid phosphatase (TRAP), which is the marker of active osteoclasts. We found that authentic SARS-CoV-2 infection prohibited the production of TRAP in femur (Figure 7G,H), suggesting of an inhibitory effect on osteoclast differentiation. These results along with the ex vivo observations indicated that SARS-CoV-2 infection disrupted BMM-to-osteoclast differentiation, and potentially had an impact on bone homeostasis (Figure 7I).

3. Discussion

In this study, we characterized SARS-CoV-2 infection in BMMs and demonstrated that NRP1 played a critical role during virus entry. This work would be the first step toward understanding the causal link between SARS-CoV-2 infection and bone metabolism. A major challenge to examine the effects of SARS-CoV-2 infection on the skeleton system lies in that there is often lag time between the occurrence of viral infection and detectable disorders of bone metabolism such as osteoporosis or osteopetrosis, though the impact can be long-lasting.^[8] Importantly, SARS-CoV-2-associated disorders of bone metabolism is supported by the clinical observations that COVID-19 patients are characterized with disorders of blood calcium and phosphorus.^[12]

ACE2 is widely accepted as the entry receptor for SARS-CoV-2. The spike protein of SARS-CoV-2 has a polybasic RRAR (Arg-Arg-Ala-Arg) motif at the boundary of S1 and S2 subunits. During the maturation process, S1 and S2 subunits are cleaved into two polypeptide chains by furin.^[41] S1 subunit binds to ACE2^[33] through RBD domain and S2 mediates membrane fusion following the cleavage by TMPRSS2.^[37] In recent studies, NRP1 has been proposed as an entry receptor for SARS-CoV-2 in certain cell hosts.^[30,31] NRP1 is an important molecule for regulating the maturation of CNS^[34] and may facilitate the spreading of SARS-CoV-2 from olfactory bulb to CNS.^[30,42] NRP1 has been reported to have high expression in infected olfactory epithelial cells of COVID-19 patients.^[30,31] Our study has demonstrated that NRP1, rather than ACE2, played a critical role during SARS-CoV-2 infection in BMMs. Unlike human and mouse ACE2,^[43] human and mouse NRP1 has minimum structural difference, justifying the use of mouse BMMs to understand SARS-CoV-2 infection in human BMMs. Intriguingly, NRP1 expression was also detected in brain macrophages. Unlike BMMs where NRP1 had relatively constant expression, brain macrophages exhibited aging or maturation-associated increase of NRP1 expression. These results may be correlated with the clinical observations that SARS-CoV-2 can infect both young and elder people but cause higher mortality in the latter.^[44]

A recent study^[39] has reported that SARS-CoV-2 infection can increase osteoclast differentiation and cause bone mass loss. However, this study relied on a hACE2 transgenic mouse model. Because we clearly demonstrated that NRP1 rather than ACE2 mediates SARS-CoV-2 infection in BMMs, the use of a hACE2

transgenic mouse model can be misleading. The present study using a Beta strain (B.1.351) virus, which can infect wild-type mouse without the need of hACE2 transduction or expression, showed that SARS-CoV-2 infection in BMMs in fact decreased osteoclast differentiation. The apparently discrepant conclusion between the present and previous studies arises from the use of different mouse models. These results have also cautioned that in the future studies of SARS-CoV-2 infection in macrophages the receptor utility should be carefully considered.

In addition, similar to SARS-CoV,^[45] SARS-CoV-2 can take advantage of both TMPRSS2 and endosomal cysteine proteases cathepsin B and L in host cells to prime S protein.^[37] In TMPRSS2 negative cells, Cathepsins B/L seem more predominant in regulating SARS-CoV-2 entry.^[37] Interestingly, we found in this study that BMMs had little TMPRSS2 expression but high Cathepsin B/L expression. Cathepsin B/L expression was also found to be associated with NRP1 expression, both of which were decreased during BMM-to-osteoclast differentiation. Therefore, the present and previous studies collectively indicated that the priming process of SARS-CoV-2 spike proteins might be also correlated with the utility of entry receptors.

Our study provided preliminary evidence that authentic SARS-CoV-2 infection might affect BMM-to-osteoclast differentiation, as evidenced by perturbed TRAP expression. Additional experiments including micro-computed tomography are needed to characterize the impact of SARS-CoV-2 infection on bone homeostasis.^[13] Nevertheless, one challenge for these experiments is the lack of appropriate animal models. Existing mouse models of SARS-CoV-2 infection do not support persistent infection, with a short duration time of a few days. In future studies, more appropriate animal models such as provocative model or persistent infection model should be developed to understand the long-term effects of SARS-CoV-2 infection on bone homeostasis. In addition, our study has shown that blockade of NRP1 can significantly inhibit SARS-CoV-2 infection on BMMs. Therefore, development of more appropriate animal models could also help understand whether targeting NRP1 is a viable approach to COVID-19 treatment.^[46] Moreover, it would be interesting to investigate the relationship between the pathologies of ACE2- and NRP1-mediated infections with appropriate animal models. Particularly, under clinical conditions SARS-CoV-2 infection in human can be triggered with a limited virus inoculum. It is thus important to investigate the roles of ACE and NRP1 in determining the cell and tissue specificities of SARS-CoV-2 infection at the early stage.

4. Conclusion

In summary, we have shown that SARS-CoV-2 can infect BMMs in an NRP1-dependent manner and that this infection can inhibit BMM-to-osteoclast differentiation. Our study provides a possible explanation for disordered calcium and phosphorus metabolisms in COVID-19 patients.

5. Experimental Section

Cell Culture: Human BMMs were collected from discarded bone tissues after total hip replacement surgery, and all procedures involving

mice including BMM isolation were approved by ethics committee of the Shanghai Jiao Tong University Affiliated Shanghai Sixth People's Hospital under the approval number of 2020-KY-16 (K) and 2021-142, and the informed consent of all participating subjects was obtained. BMMs were obtained from human or mice bone marrows in the presence of human or mice M-CSF (30 ng mL⁻¹), and osteoclasts were differentiated from BMMs following the stimulation using human or mouse RANKL (100 ng mL⁻¹). BMMs were grown in Minimum Essential Media (alpha-MEM, Thermo) supplemented with 10% fetal bovine serum (FBS, Thermo) and 1% penicillin-streptomycin (Thermo) and maintained at 37 °C in a fully humidified incubator containing 5% CO₂.^[26,27] HEK293T cells were obtained from the Cell Bank of Shanghai Institutes for Biological Science (SIBS) and were validated by VivaCell Biosciences (Shanghai, China), and were grown in Dulbecco's modified Eagle's medium (DMEM, Thermo) supplemented with 10% fetal bovine serum (FBS, Thermo) and 1% penicillin-streptomycin (P/S, Thermo) and maintained at 37 °C in a fully humidified incubator containing 5% CO₂. Vero E6 cells (derived from African Green monkey kidney) were grown in (DMEM, Thermo) supplemented with 10% FBS (Thermo) and 1% P/S (Thermo). All cells were confirmed by PCR to be free of mycoplasma contamination.

Authentic SARS-CoV-2 Infection: The SARS-CoV-2 strain used in this study was isolated from COVID-19 patients in Guangzhou (Accession numbers: MT123290), and passaged on African green monkey kidney-derived Vero E6 cells. Vero E6 were grown in Dulbecco's modified Eagle's medium (DMEM, Gibco, Grand Island, NY) supplemented with 10% FBS. BMMs were infected with SARS-CoV-2 at an MOI of 0.1 or 0.5 for 1–3 days. To analyze the kinetics of viral replication, culture supernatants and cells were harvested at the indicated time points and infectious virus was titrated using a focus forming assay (FFA, see below). Collected cells were lysed using TRIzol and fixed using 4% paraformaldehyde (PFA).

Focus Forming Assay (FFA): Vero E6 cells were seeded on to 96-well plates one day before infection. Virus culture was diluted in 1:10 dilution and inoculated on to Vero E6 cells at 37 °C for 1 h. The virus-containing medium was removed and then 1.6% carboxymethylcellulose was added. After 24 h after infection, cells were fixed with 4% paraformaldehyde and permeabilized with 0.2% Triton X-100. Cells were then incubated with a rabbit anti-SARS-CoV/SARS-CoV-2 nucleocapsid protein polyclonal antibody (Cat. No.: 40143-T62, Sino Biological, Inc., Beijing), followed by an HRP-labeled goat anti-rabbit secondary antibody (Cat. No.: 111-035-144, Jackson ImmunoResearch Laboratories, Inc., West Grove, PA). The foci were visualized by TrueBlue Peroxidase Substrate (KPL, Gaithersburg, MD), and counted with an ELISPOT reader (Cellular Technology Ltd., Cleveland, OH). Viral titers were calculated as FFU per mL.

SARS-CoV-2 Infection in Balb/c Mouse: hACE2 transduction model of SARS-CoV-2 infection in Balb/c mice was conducted as previously described.^[24] Briefly, mice were transduced with 2.5×10^8 FFU of Ad5-ACE2 intranasally. Five days post transduction, mice were infected with wild-type SARS-CoV-2 (Accession No.: MT123290; 1×10^5 PFU) intranasally. At day 2 post-infection, lung and bone were harvested, and fixed in formalin.

For infection with beta strain (B.1.351), wild-type Balb/c mice were infected with the virus intranasally and at three days post infection, femur bones were harvested. Bone marrow from forelimb and femur were harvested and lysed using TRIzol lysis buffer. SARS-CoV-2 infection was conducted in the Biosafety Level 3 (BSL3) Laboratories of Guangzhou Customs District Technology Center. All protocols were approved by the Institutional Animal Care and Use Committees of Guangzhou Medical University.

Production, Infection, and Neutralization of SARS-CoV-2 Pseudovirus: HEK293T cells were transfected with psPAX, plentiv2-Tdtomato and plasmid that carried SARS-CoV-2 S gene or empty vector using Lipofectamine 3000 (Thermo). The endoplasmic reticulum (ER) signal was removed from S gene to enhance the packaging efficiency of pseudovirus.^[38,47] Codon-optimized DNA sequences of S genes were listed in Table S1 (Supporting Information). At 48 h after transfection, supernatant containing pseudovirions was harvested by centrifugation at 2000 rpm for 10 min and concentrated by Optima XPN-100

Ultracentrifuge (Beckman Coulter, California, USA). For pseudovirus infection, BMMs were seeded on to 6- or 24-well plates (2×10^5 or 4×10^4 cells per well) for 24 h, and infected with pseudovirus for 24 h in the presence of polybrene (10 µg mL⁻¹, Merck, Darmstadt, Germany). BMMs were washed with PBS for three times at 24 h after infection, and then fixed using 4% PFA for fluorescence detection or lysed using TRIzol (Thermo) for RNA extraction.

For neutralizing experiments, SARS-CoV-2 pseudovirus were pretreated with serially diluted anti-S1 neutralizing antibody (Cat. 40592-R001, Sino Biological Inc., China) for 1 h, and then virus-antibody mixture was added onto BMMs on a 12-well plate with coated polybrene (10 µg mL⁻¹, Merck, Darmstadt, Germany). At 48 h post-infection, cells were washed with PBS for three times and then lysed with TRIzol (Thermo) for RNA extraction. Gene expression was quantified using RT-qPCR.

Immunofluorescence: Cells were cultured in coverslips (ProSciTech), and fixed in 4% PFA for 20 min. After permeabilizing in 0.1% Triton X100 in PBS for 5 min, cells were incubated with 3% BSAPBS for 30 min to block nonspecific antibody binding and then incubated with SARS-CoV-2 nucleocapsid protein antibody (Sino Biological), followed by incubating with Alexa Fluor 488 (Thermo). BMMs were labeled by F4/80 antibody (Abcam), followed by incubating with Cy3-labeled Goat Anti-Rat IgG(H+L) (Beyotime). Nucleus was stained with DAPI (Sigma), and actin cytoskeleton with rhodamine phalloidin (Thermo) or Alexa Fluor 647 phalloidin (Thermo) for 45 min. Immunostained cells were mounted by ProLong Diamond antifade medium (Invitrogen). Images were acquired by Zeiss LSM 710 confocal microscope with ECPlanNeofluar 63x oil immersion objective, digital images were acquired by ZEISS ZEN microscope software. Fiji (National Institutes of Health) was employed to analyze and assemble images.

Immunoblotting: Cell lysate was extracted by incubating in lysis buffer (Sigma) with protease inhibitor (Roche) and a phosphatase inhibitor cocktail (Sigma) for 30 min at 4 °C, and diluted with $4 \times$ SDS sampling buffer and boiled for 5 min. For each sample, proteins were fractionated on SDS-polyacrylamide gel electrophoresis gel and transferred to a nitrocellulose membrane (Millipore). Membranes were incubated with primary antibodies, including actin JLA20 antibody (Developmental Studies Hybridoma Bank), Neuropilin-1 antibody (Novus Biologicals). Proteins were visualized by enhanced chemiluminescence and autoradiography (FujiFilm LAS3000/4000 Gel Documentation System).

Real-Time Quantitative PCR: Total RNA was purified using TRIzol (Thermo), chloroform (Titan), and isopropanol precipitation. RNA was then reverse transcribed into cDNA by PrimeScript RT reagent Kit with gDNA Eraser (Takara Bio Inc.). Gene mRNA levels were determined using SYBR green dye on Applied Biosystems Q6 Real-Time PCR cycler (Thermo) and specific primers (Table S2, Supporting Information). All SYBR Green primers were validated with dissociation curves. The expression of genes was normalized to β -actin.

Gene Knockdown Using shRNA: ShRNA-NC (negative control) or shRNA-Nrp1 were synthesized, cloned into pLenti-vector (Shanghai GenePharma Co., Ltd, China) and packaged into lentivirus through co-transfection with PMD2G and PsPAX plasmids in HEK293T cells (Table S3, Supporting Information). BMMs in 12-well plate were infected with shRNA-NC or shRNA-Nrp1 lentivirus in the presence of 10 µg mL⁻¹ of polybrene for 48 h. Then cells were further infected by pseudovirus. At 48 h post-infection, cells were washed with PBS for three times and collected for RNA extraction (TRIzol, Thermo) and protein extraction (RIPA, thermo) or trypsinized for flow cytometry analysis.

SMART-Seq: Total RNA of BMMs was extracted using TRIzol (Invitrogen), and then quantified (NanoDrop, Thermo). For SMARTer cDNA synthesis, a modified oligo(dT) primer was employed. When SMARTScribe Reverse Transcriptase reaches the 5' end of the mRNA, the enzyme's terminal transferase activity adds a few additional nucleotides to the 3' end of the cDNA. Designed SMARTer Oligonucleotide base-pairs with the non-template nucleotide stretch create an extended template to enable SMARTScribe RT to continue replicating to the end of the oligonucleotide. sscDNA was amplified by LD PCR to get enough cDNA. cDNA was fragmented by dsDNA Fragmentase (NEB, M0348S). For library construction, blunt-end DNA fragments were generated using

a combination of fill-in reactions and exonuclease activity. Paired-end sequencing was performed on an Illumina Novaseq 6000 (LC Sciences, USA) following the vendor's recommended protocol.

Single-Cell RNA Sequencing (scRNA-Seq): scRNA-Seq experiment was performed by NovelBio Bio-Pharm Technology Co., Ltd. Bone marrow was flushed and kept in MACS Tissue Storage Solution (Miltenyi Biotec). Samples were sieved through 40 μm cell strainers, and centrifuged at 300 g for 5 min. Pelleted cells were suspended in red blood cell lysis buffer (Miltenyi Biotec) for lysing red blood cells. Ex vivo cultured BMMs were washed with 0.04% BSA-PBS, trypsinized and re-suspended. Brain tissues were surgically removed and minced into small pieces ($\approx 1\text{ mm}^3$) on ice and digested by 200 U mL^{-1} Papine (Diamond) and Cysteine-HCL (Sigma). Then samples were sieved through 70 μm cell strainers, centrifuged at 300 g for 10 min, and further cleaned for red blood cells using red blood cell lysis buffer (Miltenyi Biotec). Countstar Fluorescence Cell Analyzer was used for single cells viability assessment, and live cells were further enriched by MACS dead cell removal kit (Miltenyi Biotec).

The scRNA-Seq libraries were generated by 10X Genomics Chromium Controller Instrument and Chromium Single Cell 3'V3.1 Reagent Kits (10X Genomics, Pleasanton, CA). Cells were concentrated to 1000 cells μL^{-1} and ≈ 8000 cells were loaded into each channel to generate single-cell Gel Bead-In-Emulsions (GEMs), which results in expected mRNA barcoding of 6000 single-cells for each sample. After the reverse transcription, GEMs were broken and barcoded-cDNA was purified and amplified. The amplified barcoded cDNA was fragmented, A-tailed, ligated with adaptors and amplified by index PCR. Final libraries were quantified using the Qubit High Sensitivity DNA assay (Thermo) and the size distribution of the libraries were determined using a High Sensitivity DNA chip on a Bioanalyzer 2200 (Agilent). All libraries were sequenced by illumina sequencer (Illumina) on a 150 bp paired-end run.

Fastp^[48] was applied for filtering the adaptor sequence and removed the low quality reads. Then the feature-barcode matrices were obtained by aligning reads to the mouse genome (GRCm38 Ensemble: version 92) using CellRanger v3.1.0. Cells contained over 200 expressed genes and mitochondria UMI rate below 20% passed the cell quality filtering, and mitochondria genes were removed in the expression table. Seurat package (version: 2.3.4) was used for cell normalization and regression. Pearson correlation analysis (PCA) was constructed based on the scaled data with top 2000 high variable genes and top 10 principals were used for UMAP construction. The unsupervised cell cluster results were acquired using graph-based cluster method (resolution = 0.8), and the marker genes were calculated by FindAllMarkers function with wilcox rank sum test algorithm under the following criteria: 1. $\text{InFC} > 0.25$; 2. $p\text{ value} < 0.05$; 3. $\text{min.pct} > 0.1$.

Neutralizing Experiments Using Soluble S1 and RBD Recombinant Proteins: BMMs cells in 12-well plate were pretreated with serially diluted S1 (Cat. Z03501-100, Genescript Inc., China) or RBD recombinant protein (Cat. 40592-V08H, Sino Biological Inc., China) for 1 h. The cells were infected with authentic SARS-CoV-2 or pseudovirus for 48 h. Cells were washed with PBS for three times and then lysed with TRIzol (Thermo) for RNA extraction. The genes expression was determined using RT-qPCR.

Pseudovirus Attachment and Entry Assays: For pseudovirus attachment, BMMs were incubated with pseudovirus in cold medium on ice for 1 h, washed with PBS for three times and then collected for RNA extraction using TRIzol (Thermo). For pseudovirus entry, BMMs were incubated with pseudovirus in cold medium for 1 h, washed with PBS for three times and then treated with pre-warmed medium for 40 min. Then cells were washed with PBS for three times, treated with 0.25% trypsin (Thermo) for 5 min to remove surface-attached viral particles and the cells were collected for RNA extraction using TRIzol (Thermo). TdTomato expression was determined using RT-qPCR.

Flow Cytometry Experiments: Bone marrow cells were treated by M-CSF, or BMMs were infected by pseudovirus, and then cells were washed with PBS for three times and trypsinized into single cells. Flow cytometry experiments were carried out using CytoFLEX (Beckman). The data was analyzed using CytExpert software version 2.4.

TRAP Staining: Cells were cultured in coverslips (ProSciTech), and fixed in 4% PFA for 20 min. Then the slips were immersed in fixative

solution for 30 s and then rinsed for three times with deionized water. The staining solution contained diazotized Fast Garnet GBC Solution (7.0 mg mL^{-1} Fast Garnet GBC Base Solution, Catalog No. 3872-10 mL, Sigma-Aldrich, and 0.1 M sodium nitrite solution, Catalog No. 914-10 mL, Sigma-Aldrich, with proportion of 1:1), 12.5 mg mL^{-1} naphthol AS-BI phosphate solution (Catalog No. 3871-10 mL^{-1} , Sigma-Aldrich), 2.5 M acetate solution (Catalog No. 3863-50 mL, Sigma-Aldrich), 0.335 M tartrate solution (Catalog No. 3873-10 mL, Sigma-Aldrich). The slips were immersed in the staining solution for 20 min and then rinsed with deionized water. The mounting medium was ProLong Diamond Antifade Mountant (2086315, Invitrogen, USA). Images of BMMs and osteoclasts were acquired by Tissue FAXS Plus Basic microscope (TissueGnostics GmbH, Austria).

Tibia paraffin blocks were serial sectioned (7 μm), and stained with TRAP staining (Servicebio G1050-50T) and hematoxylin (Servicebio G1004) following the manufacturer's instructions.

Statistical Analysis: Unless noted otherwise, none of the data were excluded from each experiment. The data were graphed and statistically analyzed using GraphPad Prism 8.0. RT-qPCR data are represented as mean \pm standard deviation. The sample size was indicated for each experiment in figure legend. Statistical difference is determined using two-tailed Student's t test. For scRNA-Seq data wilcox rank sum test algorithm was employed under the following criteria: 1. $\text{InFC} > 0.25$; 2. $p\text{ value} < 0.05$; 3. $\text{min.pct} > 0.1$. For SMART-Seq, differentially expressed mRNAs and genes were selected with $\log_2(\text{fold change}) > 1$ or $\log_2(\text{fold change}) < -1$ and with statistical significance ($p\text{ value} < 0.05$) by R package.

Supporting Information

Supporting Information is available from the Wiley Online Library or from the author.

Acknowledgements

The authors thank Dr. Lichun Jiang and Dr. Wei Wang from High-throughput Screening (HTS) Platform at Shanghai Institute for Advanced Immunochemical Studies (SIAIS), ShanghaiTech University for the support of IF experiments and Biomedical Big Data Platform for the analyses of RNA-Seq data. This work was supported by National Natural Science Foundation of China (81820108020 to C.Q.Z.; 82002339 to J.J.G.; 82025001 to J.C.Z.), National Key R&D Program of China International Collaboration Project (Grant No. 2018YFE0200402 to J.L., 2018YFC1106300 to C.Q.Z.), the emergency grants for prevention and control of SARS-CoV-2 of Ministry of Science and Technology of Guangdong province (2020B1111330001 to J.C.Z.), Zhangjiang National Innovation Demonstration Zone (ZJ2020-ZD-004 to J.L.), Guangzhou Institute of Respiratory Health Open Project (Funds provided by China Evergrande Group)-Project No. (2020GIRHHMS24), China Postdoctoral Science Foundation (2017M621551 to H.M.), ShanghaiTech University Startup Fund (2019F0301-000-01 to J.L.), and Shanghai Sixth People's Hospital Scientific Research Foundation to J.J.G.

Conflict of Interest

The authors declare no conflict of interest.

Author Contributions

J.G., H.M., J.S., and H.L. contributed equally to this work. J.L., C.Q.Z., J.C.Z., and J.J.G. conceived, designed, and supervised the study. J.C.Z. supervised the authentic SARS-CoV-2 work and J.S. performed the

infection experiments with assistance from Y.H.T and L.W.D. J.J.G., H.M., and H.L. performed confocal imaging, SARS-CoV-2 pseudovirus, cell culture, and differentiation experiments. Y.G.H., D.L.L., Y.D.P., Q.Y.W., Y.S.G., and K.S. conducted immunoblotting, immunostaining and RT-QPCR. J.J.G. J.L., H.M., C.Q.Z., and J.C.Z. analyzed the data and wrote the manuscript.

Data Availability Statement

The data that support the findings of this study are available from the corresponding author upon reasonable request.

Keywords

bone marrow-derived macrophages, neuropilin-1, osteoclast differentiation, severe acute respiratory syndrome coronavirus 2

Received: January 13, 2022

Revised: January 25, 2022

Published online: February 23, 2022

- [1] WHO, WHO webpage, **2022**, <https://covid19.who.int/> (accessed: January, 2022).
- [2] C. Huang, Y. Wang, X. Li, L. Ren, J. Zhao, Y. Hu, L. Zhang, G. Fan, J. Xu, X. Gu, Z. Cheng, T. Yu, J. Xia, Y. Wei, W. Wu, X. Xie, W. Yin, H. Li, M. Liu, Y. Xiao, H. Gao, L. Guo, J. Xie, G. Wang, R. Jiang, Z. Gao, Q. Jin, J. Wang, B. Cao, *Lancet* **2020**, 395, 497.
- [3] N. Zhu, D. Zhang, W. Wang, X. Li, B. Yang, J. Song, X. Zhao, B. Huang, W. Shi, R. Lu, P. Niu, F. Zhan, X. Ma, D. Wang, W. Xu, G. Wu, G. F. Gao, W. Tan, *2019 N. Engl. J. Med.* **2020**, 382, 727.
- [4] X. Yang, Y. Yu, J. Xu, H. Shu, J. Xia, H. Liu, Y. Wu, L. Zhang, Z. Yu, M. Fang, T. Yu, Y. Wang, S. Pan, X. Zou, S. Yuan, Y. Shang, *Lancet Respir. Med.* **2020**, 8, 475.
- [5] K. S. Cheung, I. F. N. Hung, P. P. Y. Chan, K. C. Lung, E. Tso, R. Liu, Y. Y. Ng, M. Y. Chu, T. W. H. Chung, A. R. Tam, C. C. Y. Yip, K. H. Leung, A. Y. Fung, R. R. Zhang, Y. Lin, H. M. Cheng, A. J. X. Zhang, K. K. W. To, K. H. Chan, K. Y. Yuen, W. K. Leung, *Gastroenterology* **2020**, 159, 81.
- [6] A. Morris, *Nat. Rev. Endocrinol.* **2021**, 17, 192.
- [7] L. Mao, H. Jin, M. Wang, Y. Hu, S. Chen, Q. He, J. Chang, C. Hong, Y. Zhou, D. Wang, X. Miao, Y. Li, B. Hu, *JAMA Neurol.* **2020**, 77, 683.
- [8] P. Zhang, J. Li, H. Liu, N. Han, J. Ju, Y. Kou, L. Chen, M. Jiang, F. Pan, Y. Zheng, Z. Gao, B. Jiang, *Bone Res.* **2020**, 8, 8.
- [9] S. Kopic, J. P. Geibel, *Physiol. Rev.* **2013**, 93, 189.
- [10] J. A. Deodatus, S. A. Kooistra, S. Kurstjens, J. C. L. Mossink, J. D. van Dijk, P. H. P. Groeneveld, B. van der Kolk, *Infect. Dis.* **2022**, 54, 90.
- [11] L. Di Filippo, M. Doga, S. Frara, A. Giustina, *Rev. Endocr. Metab. Disord.* **2021**, 1, <https://doi.org/10.1007/s11154-021-09655-z>.
- [12] C. Yang, X. Ma, J. Wu, J. Han, Z. Zheng, H. Duan, Q. Liu, C. Wu, Y. Dong, L. Dong, *J. Med. Virol.* **2021**, 93, 1639.
- [13] C. E. Jacome-Galarza, G. I. Percin, J. T. Muller, E. Mass, T. Lazarov, J. Eitler, M. Rauner, V. K. Yadav, L. Crozet, M. Bohm, P. L. Loyher, G. Karsenty, C. Waskow, F. Geissmann, *Nature* **2019**, 568, 541.
- [14] M. Kawase, M. Tsuda, T. Matsuo, *J. Bone Miner. Res.* **1989**, 4, 359.
- [15] J. Li, I. Sarosi, X. Q. Yan, S. Morony, C. Capparelli, H. L. Tan, S. McCabe, R. Elliott, S. Scully, G. Van, S. Kaufman, S. C. Juan, Y. Sun, J. Tarpley, L. Martin, K. Christensen, J. McCabe, P. Kostenuik, H. Hsu, F. Fletcher, C. R. Dunstan, D. L. Lacey, W. J. Boyle, *Proc. Natl. Acad. Sci. U. S. A.* **2000**, 97, 1566.
- [16] J. R. Edwards, G. R. Mundy, *Nat. Rev. Rheumatol.* **2011**, 7, 235.
- [17] Y. Yao, X. Cai, F. Ren, Y. Ye, F. Wang, C. Zheng, Y. Qian, M. Zhang, *Front. Immunol.* **2021**, 12, 664871.
- [18] K. Ikeda, S. Takeshita, *J. Biochem.* **2016**, 159, 1.
- [19] R. Channappanavar, S. Perlman, *Semin. Immunopathol.* **2017**, 39, 529.
- [20] R. Channappanavar, A. R. Fehr, R. Vijay, M. Mack, J. Zhao, D. K. Meyerholz, S. Perlman, *Cell Host Microbe* **2016**, 19, 181.
- [21] M. Merad, J. C. Martin, *Nat. Rev. Immunol.* **2020**, 20, 355.
- [22] J. J. Mourad, B. I. Levy, *Nat. Rev. Cardiol.* **2020**, 17, 313.
- [23] A. R. Bowden, D. A. Morales-Juarez, M. Sczaniecka-Clift, M. M. Agudo, N. Lukashchuk, J. C. Thomas, S. P. Jackson, *eLife* **2020**, 9, e55325.
- [24] J. Sun, Z. Zhuang, J. Zheng, K. Li, R. L. Wong, D. Liu, J. Huang, J. He, A. Zhu, J. Zhao, X. Li, Y. Xi, R. Chen, A. N. Alshukairi, Z. Chen, Z. Zhang, C. Chen, X. Huang, F. Li, X. Lai, D. Chen, L. Wen, J. Zhuo, Y. Zhang, Y. Wang, S. Huang, J. Dai, Y. Shi, K. Zheng, M. R. Leidinger, et al., *Cell* **2020**, 182, 734.
- [25] U. M. Gundra, N. M. Girgis, M. A. Gonzalez, M. San Tang, H. J. P. Van Der Zande, J. D. Lin, M. Ouimet, L. J. Ma, J. Poles, N. Vozhilla, E. A. Fisher, K. J. Moore, P. Loke, *Nat. Immunol.* **2017**, 18, 642.
- [26] S. Manzanero, *Methods Mol. Biol.* **2012**, 844, 177.
- [27] A. Assouvie, L. P. Daley-Bauer, G. Rousselet, *Methods Mol. Biol.* **2018**, 1784, 29.
- [28] M. Yilla, B. H. Harcourt, C. J. Hickman, M. McGrew, A. Tamin, C. S. Goldsmith, W. J. Bellini, L. J. Anderson, *Virus Res.* **2005**, 107, 93.
- [29] C. Y. Cheung, L. L. Poon, I. H. Ng, W. Luk, S. F. Sia, M. H. Wu, K. H. Chan, K. Y. Yuen, S. Gordon, Y. Guan, J. S. Peiris, *J. Virol.* **2005**, 79, 7819.
- [30] L. Cantuti-Castelvetri, R. Ojha, L. D. Pedro, M. Djannatian, J. Franz, S. Kuivanen, F. van der Meer, K. Kallio, T. Kaya, M. Anastasina, T. Smura, L. Levanov, L. Szivovics, A. Tobi, H. Kallio-Kokko, P. Österlund, M. Joensuu, F. A. Meunier, S. J. Butcher, M. S. Winkler, B. Mollenhauer, A. Helenius, O. Gokce, T. Teesalu, J. Hepojoki, O. Vapalahti, C. Stadelmann, G. Balistreri, M. Simons, *Science* **2020**, 370, 856.
- [31] J. L. Daly, B. Simonetti, K. Klein, K. E. Chen, M. K. Williamson, C. Antón-Plágaro, D. K. Shoemark, L. Simón-Gracia, M. Bauer, R. Hollandi, U. F. Greber, P. Horvath, R. B. Sessions, A. Helenius, J. A. Hiscox, T. Teesalu, D. A. Matthews, A. D. Davidson, B. M. Collins, P. J. Cullen, Y. Yamauchi, *Science* **2020**, 370, 861.
- [32] M. V. Gelfand, N. Hagan, A. Tata, W. J. Oh, B. Lacoste, K. T. Kang, J. Kopycinska, J. Bischoff, J. H. Wang, C. Gu, *eLife* **2014**, 3, e03720.
- [33] Q. Wang, Y. Zhang, L. Wu, S. Niu, C. Song, Z. Zhang, G. Lu, C. Qiao, Y. Hu, K. Y. Yuen, Q. Wang, H. Zhou, J. Yan, J. Qi, *Cell* **2020**, 181, 894.
- [34] B. S. Mayi, J. A. Leibowitz, A. T. Woods, K. A. Ammon, A. E. Liu, A. Raja, *PLoS Pathog.* **2021**, 17, e1009153.
- [35] F. Zhou, T. Yu, R. Du, G. Fan, Y. Liu, Z. Liu, J. Xiang, Y. Wang, B. Song, X. Gu, L. Guan, Y. Wei, H. Li, X. Wu, J. Xu, S. Tu, Y. Zhang, H. Chen, B. Cao, *Lancet* **2020**, 395, 1054.
- [36] P. Padmanabhan, R. Desikan, N. M. Dixit, *PLoS Comput. Biol.* **2020**, 16, e1008461.
- [37] M. Hoffmann, H. Kleine-Weber, S. Schroeder, N. Krüger, T. Herrler, S. Erichsen, T. S. Schiergens, G. Herrler, N. H. Wu, A. Nitsche, M. A. Müller, C. Drosten, S. Pöhlmann, *Cell* **2020**, 181, 271.
- [38] X. Ou, Y. Liu, X. Lei, P. Li, D. Mi, L. Ren, L. Guo, R. Guo, T. Chen, J. Hu, Z. Xiang, Z. Mu, X. Chen, J. Chen, K. Hu, Q. Jin, J. Wang, Z. Qian, *Nat. Commun.* **2020**, 11, 1620.
- [39] O. D. Awosanya, C. E. Dallou, R. J. Blosser, U. C. Dadwal, M. Carozza, K. Boschen, M. J. Klemsz, N. A. Johnston, A. Bruzzaniti, C. M. Robinson, E. F. Srouf, M. A. Kacena, *Bone* **2021**, 154, 116227.
- [40] Xavier M., M. Prot, L. Levillayer, E. B. Salazar, G. Jouvion, L. Conquet, F. Donati, *bioRxiv* **2021**, doi: <https://doi.org/10.1101/2021.03.18.436013>.

- [41] A. C. Walls, Y. J. Park, M. A. Tortorici, A. Wall, A. T. McGuire, D. Veessler, *Cell* **2020**, *181*, 281.
- [42] M. K. M. Karuppan, D. Devadoss, M. Nair, H. S. Chand, M. K. Lakshmana, *Mol. Neurobiol.* **2021**, *58*, 2465.
- [43] C. Muñoz-Fontela, W. E. Dowling, S. G. P. Funnell, P. S. Gsell, A. X. Riveros-Balta, R. A. Albrecht, H. Andersen, R. S. Baric, M. W. Carroll, M. Cavaleri, C. Qin, I. Crozier, K. Dallmeier, L. de Waal, E. de Wit, L. Delang, E. Dohm, W. P. Duprex, D. Falzarano, C. L. Finch, M. B. Frieman, B. S. Graham, L. E. Gralinski, K. Guilfoyle, B. L. Haagmans, G. A. Hamilton, A. L. Hartman, S. Herfst, S. J. F. Kaptein, W. B. Klimstra, et al., *Nature* **2020**, *586*, 509.
- [44] M. O'Driscoll, G. Ribeiro Dos Santos, L. Wang, D. A. T. Cummings, A. S. Azman, J. Paireau, A. Fontanet, S. Cauchemez, H. Salje, *Nature* **2021**, *590*, 140.
- [45] G. Simmons, D. N. Gosalia, A. J. Rennekamp, J. D. Reeves, S. L. Diamond, P. Bates, *Proc. Natl. Acad. Sci. U. S. A.* **2005**, *102*, 11876.
- [46] S. Sarabipour, F. M. Gabhann, *FEBS J.* **2021**, *288*, 5122.
- [47] L. Pellegrini, A. Albecka, D. L. Mallery, M. J. Kellner, D. Paul, A. P. Carter, L. C. James, M. A. Lancaster, *Cell Stem Cell* **2020**, *27*, 951.
- [48] S. Chen, Y. Zhou, Y. Chen, J. Gu, *Bioinformatics* **2018**, *34*, i884.